applied optics

Spatial light modulator phase mask implementation of wavefront encoded 3D computational-optical microscopy

SHARON V. KING,[1,*] ANA DOBLAS,[2] NURMOHAMMED PATWARY,[1] GENARO SAAVEDRA,[2] MANUEL MARTÍNEZ-CORRAL,[2] AND CHRYSANTHE PREZA[1]

[1]The University of Memphis, Computational Imaging Research Laboratory, Department of Electrical and Computer Engineering, 206 Engineering Science, Memphis, Tennessee 38152, USA
[2]Universitat de València, 3D Imaging and Display Laboratory, Department of Optics, E-46100 Burjassot, Spain
*Corresponding author: svking@memphis.edu

Received 9 July 2015; revised 28 August 2015; accepted 6 September 2015; posted 8 September 2015 (Doc. ID 245524); published 2 October 2015

Spatial light modulator (SLM) implementation of wavefront encoding enables various types of engineered point-spread functions (PSFs), including the generalized-cubic and squared-cubic phase mask wavefront encoded (WFE) PSFs, shown to reduce the impact of sample-induced spherical aberration in fluorescence microscopy. This investigation validates dynamic experimental parameter variation of these WFE-PSFs. We find that particular design parameter bounds exist, within which the divergence of computed and experimental WFE-PSFs is of the same order of magnitude as that of computed and experimental conventional PSFs, such that model-based approaches for solving the inverse imaging problem can be applied to a wide range of SLM-WFE systems. Interferometric measurements were obtained to evaluate the SLM implementation of the numeric mask. Agreement between experiment and theory in terms of a wrapped phase, 0–2π, validates the phase mask implementation and allows characterization of the SLM response. These measurements substantiate experimental practice of computational-optical microscope imaging with an SLM-engineered PSF.

OCIS codes: (110.0110) Imaging systems; (180.0180) Microscopy; (230.6120) Spatial light modulators; (110.7348) Wavefront encoding.

http://dx.doi.org/10.1364/AO.54.008587

1. INTRODUCTION

Implementation of wavefront encoding with a spatial light modulator (SLM) offers to microscopists the possibility to switch at high speed between different wavefront encoded (WFE) imaging systems. For example, simulation shows that one set of generalized cubic phase mask (GCPM) parameters renders the encoded point-spread function (PSF) insensitive to misfocus, thereby creating an extended depth of field (EDF) system with some advantages over the one obtained with the traditional cubic phase mask (CPM) [1,2]. Another set of GCPM parameters makes the PSF insensitive to spherical aberration (SA) yet suitable for computational optical sectioning microscopy (COSM) [1]. This set of parameters creates a GCPM-PSF whose performance can be compared with PSFs created using the squared cubic (SQUBIC) phase mask [3–5]. The SQUBIC phase mask was designed to address the impact of SA on the PSF. In addition to altering imaging system properties, selection of wavefront encoding phase mask design parameters [1,5,6] determines the scale, shape, and performance of the engineered PSF.

The wavefront encoding method of PSF engineering has been successfully applied, beyond the initial concept developed by Dowski and Cathy for EDF imaging [7,8] to create a variety of microscopy modes. In EDF-WFE microscopy, the PSF is engineered to be insensitive to misfocus with a CPM. However, the wavefront encoding method is also applied in super-resolved localization microscopy, using a double helix or self-bending PSF [9,10]; in spatial light interference microscopy (SLIM), using a time-varying Zernike phase contrast PSF [11]; in spiral phase contrast microscopy, using a differentiating PSF [12]; and in polarization fluorescence microscopy using a vectorially engineered PSF [13]. EDF and double-helix PSFs can be used in tandem, provided their depth range parameters are chosen to match [14].

Each of the new wavefront encoding imaging modes listed above [7–11] has been implemented with a liquid crystal (LC)

1559-128X/15/298587-09$15/0$15.00 © 2015 Optical Society of America

SLM. The referenced methods do not use model-based algorithms for determination of 3D fluorescence distribution; therefore, validation of high-level consistency between experiment and theory in order to avoid image artifacts is not required. However, an accurate theoretical representation of experimental conditions by the PSF model is necessary in COSM in order to avoid restoration artifacts [15] because the PSF defines the system model used in solving the forward and inverse imaging problems. This requirement also applies to modified confocal microscopy, which relies on computations to obtain an improved image [16].

COSM is a method for high-resolution 3D imaging in which out-of-focus information is removed computationally by reassigning light intensity to its original source location. To address depth variability (due to the presence of sample-induced aberrations) when imaging deep in optically thick samples, we have developed restoration methods, based on maximum likelihood estimation and multiple depth-variant 3D PSFs, to estimate sample properties from an acquired image [17–19]. The use of a WFE system with reduced depth variance reduces computational resources required for this approach to solving the inverse imaging problem.

In this paper, the effectiveness of LC-SLM PSF engineering is investigated by experimentally validating the implementation of phase masks as a function of their variable design parameters. We implemented wavefront encoding for PSF engineering in a commercial upright Zeiss AxioImager microscope modified with a dual camera port and a LC-SLM adapted to the second imaging path. We effectively measured the 3D PSF by acquiring images of fluorescent beads, of unresolved size, with a high numerical aperture (NA) objective. Using data discrepancy and overlap measures, we determined that, by characterizing the SLM and taking into account its properties, inconsistency between the SLM implementation and numerical representation of a phase mask can become small enough so that numerical WFE-PSFs predict a good approximation of experimental WFE-PSFs.

The paper is organized as follows. Section 2 briefly reviews the theoretical form of three wavefront encoding phase masks of interest: CPM, GCPM, and SQUBIC. Section 3 describes methods used for verification of the SLM-WFE PSFs, the adaptation of the SLM to the microscope and experimental imaging methods, as well as information relevant to the simulated WFE-PSFs. Simulation methods are discussed in detail in previous publications [4,5]. Section 4 presents results of the SLM implementation of the three phase mask designs. Some earlier results from this study have been presented in a conference publication [20].

2. INVESTIGATED WAVEFRONT ENCODING PHASE MASKS: CPM, GCPM, AND SQUBIC

We investigated experimental SLM implementation of CPM, GCPM, and SQUBIC phase masks in a microscope. These wavefront encoding phase mask designs have been thoroughly discussed in the literature [1–3,5,–7,21–23].

The GCPM phase distribution [23] is given by

$$\varphi_{\mathrm{GCPM}}(f_x, f_y) = \alpha(f_x^3 + f_y^3) + \beta(f_x^2 f_y + f_x f_y^2). \quad (1)$$

For $\beta = 0$, GCPM is equivalent to CPM [2,22], where f_x and f_y are the normalized Cartesian coordinates of the objective exit pupil and α is the *strength* of the phase mask, which determines the axial extent of the PSF and, subsequently, the extent of the CPM-WFE system's depth of field [1,6].

The phase distribution of the SQUBIC [3,5] phase mask is given by

$$\phi_{\mathrm{SQUBIC}}(f_x, f_y) = A\left(\frac{\sqrt{1 - (f_x^2 + f_y^2)\sin^2\alpha_m} - 1}{1 - \cos\alpha_m} + 0.5\right)^3, \quad (2)$$

where A is a *strength* parameter that determines axial extent of the WFE-PSF and its invariability in the presence of SA. The parameter α_m is the maximum acceptance angle of the imaging pupil [NA $= n\sin(\alpha_m)$, where n is the refractive index (RI) of the lens' immersion medium]. For a large A, the SQUBIC phase mask creates a depth-invariant PSF in the presence of depth-induced SA that always maintains optical sectioning capability [3,5].

3. METHODS

A. Experimental PSF Acquisition

Experimental PSFs were measured by imaging 0.175 μm diameter fluorescent beads (Invitrogen Point Source Kit, P7220) with a wavelength, $\lambda_{\mathrm{peak}} = 608$ nm (Fig. 1 only) and 515 nm (all other figures and results). A dilute solution of the beads was dried on a high-precision Zeiss coverslip and then mounted either in glycerol mounting medium (Figs. 1, 4, and 5) [$n \sim 1.47$] or in optical cement (Norland 63, $n \sim 1.56$, see Fig. 6) cured under low-power diffused UV illumination for approximately 20 min. Individual beads were imaged with a $63\times/1.4$ NA oil immersion ($n = 1.515$) objective lens and a 515–565 nm emission filter (Zeiss filter set 10). At this magnification, the effective camera pixel size is 0.1 μm × 0.1 μm. Axial 2D image stacks were acquired at 0.1 μm intervals such that the effective experimental voxel size is 0.1 μm × 0.1 μm × 0.1 μm.

B. LC WFE Microscope Imaging Path

PSF engineering was implemented by adapting a WFE imaging path to a modified Zeiss AxioImager with a dual camera port configuration and identical cameras (Zeiss Axiocam MRm) to enable acquisition via the original microscope-imaging path, or the LC-WFE image path. The LC-WFE imaging path at the *side camera port* contains a unit magnification 4-f imaging system (Fig. 2) [9,20] (folded at a 20° angle) in which a LC SLM (XY Phase Series with High Speed LC and Custom 500–700 nm Dielectric Mirror Coating, Meadowlark Optics, Inc, Frederick, CO) is conjugate to the objective back focal plane. The SLM was used with a global calibration created *in situ* for 532 nm illumination at 20° incidence. This global calibration maps applied voltage to phase via fitting of measured and theoretical diffraction and was created with a set of checkerboard patterns (16 × 16 pixel blocks) with varying phase modulation depth 0 to 2π. It is possible to introduce a small magnification or adjustable zoom into the 4-f imaging system, so that the full pixel format of the SLM is illuminated

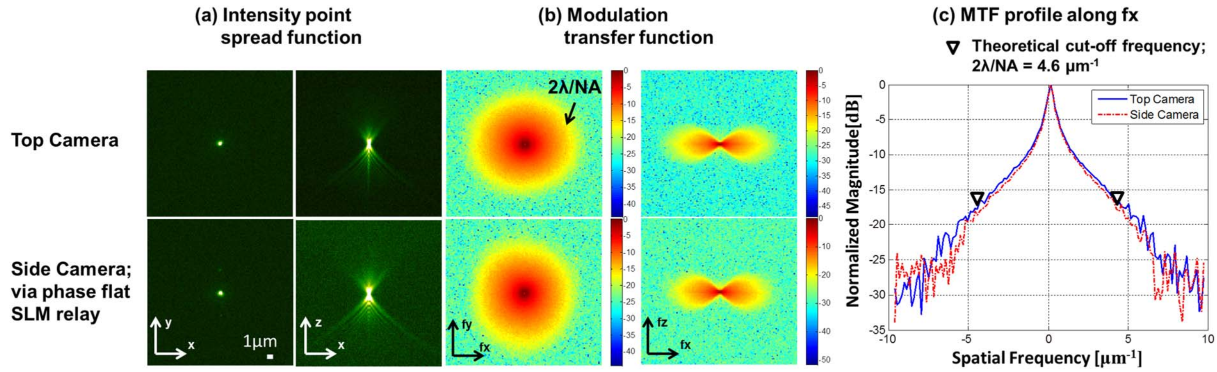

Fig. 1. Effect of SLM relay on image frequency spectrum. (a) XY and XZ sections of measured PSFs for the top and side imaging ports from images of fluorescent emission (608 nm) emitted by 0.175 μm beads obtained with a 63 × /1.4 NA oil-immersion objective lens. (b) XY and XZ sections of the 3D MTF computed from the measured PSF. An arrow indicates the theoretical cut-off frequency. (c) Vertical profiles through the MTF along f_x for $f_y = f_z = 0$. The SLM-WFE imaging path does not contribute significant aberrations to the image.

by the exit pupil aperture and the full resolution of the SLM can be used to encode the pupil phase. However, in this study, no magnification was used. This approach was taken in order to allow direct comparison between conventional and WFE imaging, without a change in image scale. Use of only a central subset of the SLM array also minimizes the effects of nonuniformity in the device [24].

Direct comparison of PSFs and their associated modulation transfer functions (MTFs) from both imaging ports shows a consistent system response that indicates the WFE imaging path does not contribute significant aberrations to the WFE image. In Fig. 1, PSF and corresponding MTF results are shown. No phase variation was applied in this case to the LC-SLM. A small extension in width of the side camera MTF is seen along the f_y direction [Fig. 1(b)]. This distortion is related to the fold angle of the LC-WFE imaging path and the elliptical projection of the pupil plane illumination image on the SLM reflection plane in the off-axis configuration. Overall, this measurement establishes a reference from which it is evident that the unmodulated WFE imaging path is very closely comparable with the conventional, clear circular aperture (CCA) system (top camera, Fig. 1); thus, subsequent WFE-PSF measurements show the result of the effects of SLM modulation.

C. Verification of Wavefront Phase from SLM: Simulation and Experiment

A modified Mach–Zehnder interferometer [Fig. 2(a)] was used to measure the phase modulation at the SLM during phase mask implementation. The experimental measurement system was also simulated with a simplified 2D scalar model in order to gain further insight into the effects of the SLM on the computed phase mask. In this model, the intensity in the 2D image resulting from the interference of two plane waves was computed using a 7125 × 7125 grid, a 1× magnification, and a 0.127 NA; the image was finally downsampled to a 256 × 256 grid. In the simulation, the sample beam interacts with the SLM. The effects of propagation, through the SLM device (diffraction and transmission), were modeled by convolution of the numeric phase mask with an empirically determined SLM response function [referred to as an SLM-modified mask, Fig. 2(c)]. Additionally, a 95% decrease in amplitude of the phase mask at the locations of the 0–2π wrapped phase was used to model absorption observed experimentally on the SLM [Fig. 2(b)].

The SLM's response function was determined using a method derived from that of Persson *et al.* [25] and reported

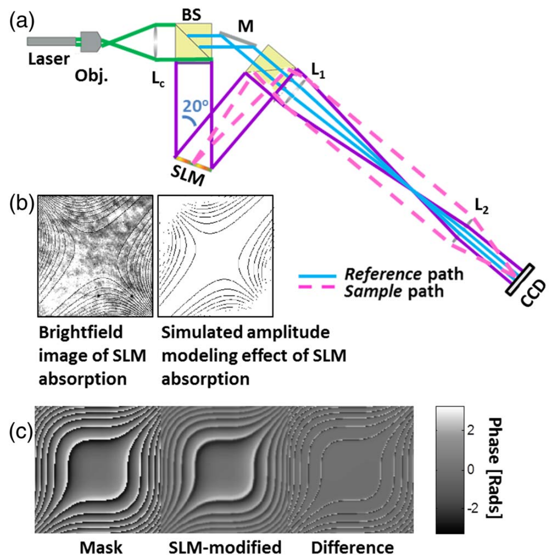

Fig. 2. Configuration for experimental and simulated measurement of the SLM-implemented phase mask. (a) Experimental Mach–Zehnder schematic. Off-axis illumination on the SLM replicates configuration used in the microscope WFE imaging path. Collimating lens, L_c; $f_c = 100$ mm; imaging lenses, L_1 and L_2; $f_1 = 100$ mm, $f_2 = 50$ mm; M, mirror; BS, beam splitter; the CCD is a Zeiss Axiocam MRm. (b) Loss in transmitted amplitude occurs at locations of 0–2π wrapped phase, evident in the brightfield image acquired from the SLM in the case of the GCPM, due to extreme changes in LC molecular orientation between adjacent pixels. The simulated image demonstrates how this loss is accounted for in phase mask comparison. (c) Effect of the SLM in the off-axis configuration is accounted for in simulation by a numeric phase mask convolved with the SLM response shown here as the SLM-modified mask in the case of the CPM.

in [26]. The SLM was addressed with binary gratings and checkerboard patterns of different modulation depths and of different periods (equal to 2–12 pixels). Following illumination of the SLM in a 20° off-axis configuration, to reproduce the configuration of the WFE system, the normalized diffracted power in the first order was measured as a function of spatial frequency and interpolated to produce a 2D SLM frequency response function. This function was used to model the spatial frequency dependence of the SLM's diffraction efficiency.

In the experimental interferometer system, the collimated output of a 4.5 mW laser diode module at 532 nm (Thorlabs, Inc., Newton, NJ) illuminates the reflective SLM interface [Fig. 2(a)] at angle of incidence approximately 20° from normal. Interference of the reflected wavefront with a plane reference wave is imaged onto a Zeiss Axiocam MRm with an approximately 2× demagnification. Measurements were acquired on an isolated optical bench, with care taken to mechanically isolate the SLM control electronics. Intensity of the reference, I_{ref}, and sample beams, I_{sple}, was captured by blocking the alternate beam path while acquiring an image. To further average temporal intensity fluctuations, 12–15 interference images were acquired for each phase mask.

The phase modulation produced by the SLM, $\varphi(x, y)$, was obtained from the simulated and experimental interference images, $I(x, y)$, by the conventional formula [27],

$$\phi(x, y) = \cos^{-1}\left(\frac{I(x, y) - I_{\mathrm{ref}}(x, y) - I_{\mathrm{sple}}(x, y)}{2\sqrt{I_{\mathrm{ref}}(x, y) I_{\mathrm{sple}}(x, y)}}\right), \quad (3)$$

where (x, y) are the pixel spatial coordinates. In the experimental case, phase modulation measurements from repeated image acquisitions were averaged, as shown in Fig. 3.

D. Simulated WFE PSFs

Simulated PSFs for conventional widefield microscopy were computed using the Gibson and Lanni PSF model [28] via the PSF computation module of the COSMOS software package [29]. PSFs were computed on a 256 × 256 × 300 grid with the same voxel size as used in the experiments (0.1 μm × 0.1 μm × 0.1 μm). The system parameters used to simulate an image of the point source were also the same as in the experiments (63 × /1.4 NA oil-immersion objective lens, $\lambda = 515$ nm), $n \sim 1.47$ (Figs. 4 and 5) or $n \sim 1.56$ (Fig. 6). WFE-PSFs were calculated using the following steps. First, the 2D Fourier transform, of the lateral planes in the 3D complex-valued CCA PSFs, was computed; thereby obtaining the conventional amplitude transfer function. Next, a 2D WFE-PSF was computed for each depth by applying the phase mask to the generalized pupil function. Finally, a 3D WFE-PSF was obtained by stacking the 2D WFE-PSFs. A mathematical description of this process is found in [1].

Three types of WFE-PSFs are reported in Section 4. One type is the ideal WFE-PSF for which the point source was located at 0 μm depth below the coverslip that exhibits no effect of SA. A second type is a WFE-PSF for which the point source was located at 25 μm below the coverslip. This depth from the coverslip was chosen empirically through a comparison study of the simulated CCA PSF and the measured CCA-PSF [20]. This study showed that an experimental CCA-PSF measurement (with $\Delta n = n_{\text{immersion-oil}} - n_{\text{mounting-medium}} = 0.05$) exhibits an asymmetrical intensity spread in the axial direction that compares best with a simulated CCA-PSF ($\Delta n = 0.05$) computed at a 25 μm depth below the coverslip. This result was determined by investigating the differences between normalized PSF intensity distributions at simulated depths in the range

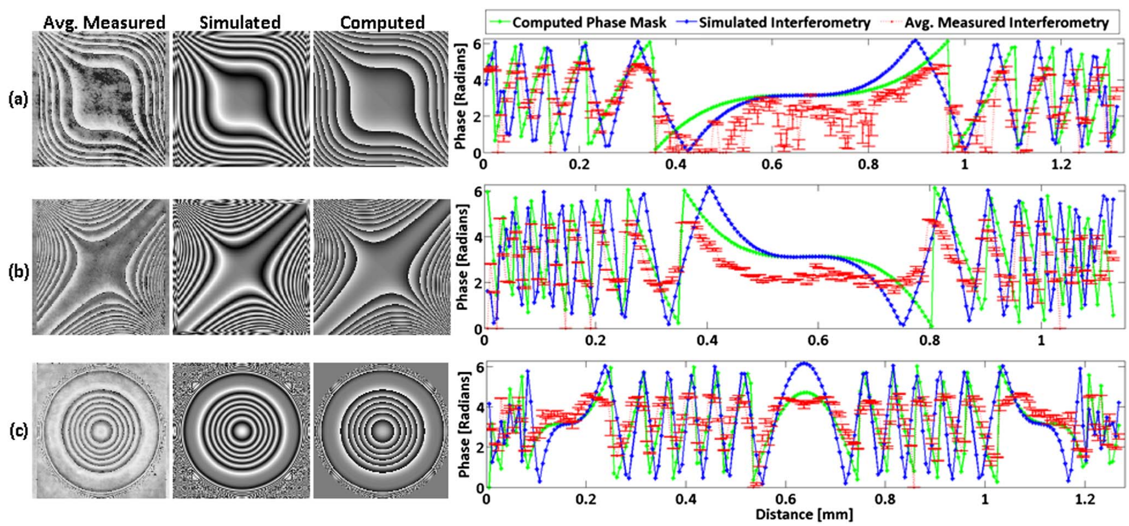

Fig. 3. Verification of wavefront phase implemented with a LC-SLM. Computed phase mask designs are compared with their SLM implementation using experimental and simulated interferometry: (a) CPM, $\alpha = 30$; (b) GCPM, $\alpha = 50$, $\beta = -50$; (c) SQUBIC, $A = 50$. Measured, simulated, and computed wrapped phase images are displayed on a minimum to maximum gray scale. Profiles, plotted to the right of the corresponding phase images, are aligned at their center point and are taken along: a diagonal direction (top right to bottom left) in the case of the CPM image; the horizontal direction in the case of GCPM; and the vertical direction in the case of the SQUBIC mask. Experimental measurement shows the average and variance (red error bars) of 12 realizations of wavefront encoding SLM phase mask modulation. The number of 0–2π wrapped phase lines in the measured, simulated, and computed cases agrees for all phase masks with some error in the pattern spatial fidelity and reduced modulation depth.

of 15–40 μm, and the experimental PSF intensity. A third type of WFE-PSF is one for which the effect of the SLM is taken into account in addition to the effects of SA at 25 μm below the coverslip. This type of WFE-PSF was computed with an SLM-modified phase mask [Fig. 2(c)], as described in Section 3.C.

E. Computation of PSF Divergence and Overlap

To assess measures of dissimilarity and overlap between experimental and simulated PSFs, Csiszár's I-divergence [30] and the correlation coefficient were computed using MATLAB (Mathworks, Inc.). I-divergence is an appropriate measure of dissimilarity when comparing non-negative functions such as probability density functions of photon distribution. The experimental and simulated intensity PSFs are interpreted as non-negative probability density functions of photon distribution. The correlation coefficient is a measure of the strength of the linear relationship between these two volumetric distributions. 3D numeric arrays representing two PSFs were first normalized by their maximum value in their respective array volume and rescaled to set the range of values to [0,1]. Then, the two arrays were registered to each other by shifting pixel coordinates such that the PSFs' structures appear aligned qualitatively. The quantitative measures listed above were then computed element-wise between the two 3D image arrays.

4. RESULTS AND DISCUSSION

A. Phase Mask Interferometry

Comparison among measured, simulated, and computed phase masks (Fig. 3) verifies the wavefront encoding SLM phase and demonstrates the difference between the phase determined by simulation and implemented in the experimental microscope. As evident from Fig. 3, the wavefront encoding SLM phase (average measured) represents the computed phase mask well in terms of the number of 0–2π wrapped phase lines and the shape of each mask design, although some discrepancy is present. Two clear differences can be observed from Fig. 3: (1) a mismatch in spatial conformation and (2) a reduction of the measured modulation depth as compared with both the computed mask and its simulated interference measurement. These differences subsequently manifest in deviation between simulated and experimental PSFs that is a source of error in restoration with COSM algorithms.

Spatial distortion in the measured masks can be seen in each case by the increased height-to-width aspect ratio of the average measured phase mask interference image compared with the computed phase mask and its simulated interference image (Fig. 3). Measured phase masks appear stretched along the vertical axis suggesting that the source of this error may be the tilted angle of the incident illumination [this is more evident in the case of the measured SQUBIC phase mask, Fig. 3(c), because it is circularly symmetric]. Profiles from these images at orthogonal directions, [Fig. 3(b) horizontal, Fig. 3(c) vertical] show that spatial distortion is primarily unidirectional and an apparent linear change in scale.

The reduced modulation depth of the SLM phase compared with that of the computed phase mask is observed in phase profiles through the interference images (Fig. 3). At locations where the computed phase mask has a modulo 2π wrapped phase, the measured phase follows the digital pattern without reaching a 2π phase delay. Two possible causes of this decrease in modulation of the SLM phase are: (1) a reduction in the total amount of SLM phase stroke due to the high angle of illumination incidence at the SLM [31] or the use of phase masks that require a high density of (modulo 2π) phase wrapping; (2) an error in the measured SLM phase due to inhomogeneity in the background normalization or residual background noise in the interferogram. The former effects, known as cross talk [31,32], are also indicated in independent experimental diffraction efficiency measurements of our LC-SLM in the off-axis configuration. These demonstrate a decrease in efficiency with increased spatial frequency of the phase pattern [25,26].

A final possible source of error, in the SQUBIC phase mask only, is due to undersampling of the high-frequency phase wrapping oscillation at the outer edge in the computed phase mask because the phase function is sampled on a grid dictated by the SLM. This undersampling can be avoided by introducing magnification into the 4-f imaging system, so that the full resolution of the SLM is used, or by using a SLM with a smaller pixel size. Exacerbating this error is the demagnification in the phase-modulated path of the experimental interferometer (see Section 4.C).

B. Boundaries of SLM Wavefront Encoding Implementation

The SLM format and its optical response place limitations on the values of the CPM, GCPM, and SQUBIC design parameters that can be implemented with high fidelity. Design parameters may be limited for four possible reasons. First, the *unwrapped* phase function can be aliased by the pixel size of the SLM (15 μm in this investigation). Second, the *unwrapped* phase function may have a maximum phase amplitude that cannot be accommodated by the phase stroke of the SLM (approximately 57λ using a phase-wrapping frequency equal to 2π radians per 4 pixels at $\lambda = 532$ nm and 20° illumination incidence). Third, the *wrapped phase* function may have a high spatial frequency of phase wrapping that suffers aliasing of phase wrapping oscillations. Finally, the *wrapped phase* function with a high spatial frequency of phase wrapping may have significantly reduced diffraction efficiency related to reduced SLM phase-modulation depth (modulation reduced by approximately 50% at a phase-wrapping frequency equal to 2π radians per 4 pixels at $\lambda = 532$ nm and 20° illumination incidence [26]).

The upper limit on values of the phase mask parameters, imposed by the SLM pixel size, can be determined from the derivative of the unwrapped phase mask. If values of the CPM, GCPM, and SQUBIC phase mask derivatives are interpreted as values of instantaneous spatial frequency, then the limiting value of the design parameters α or A in Eqs. (1) and (2), respectively, is the highest value for which the maximum value of the phase mask derivative is less than the SLM sampling frequency, which is equal to $1/15\ \mu\text{m} = 0.067\ \mu\text{m}^{-1}$.

The effect of reduced SLM phase modulation depth on the WFE-PSF is demonstrated by a series of measured CPM-PSFs with the design parameter α in the range $\alpha = 30$ to 100 (Fig. 4). As the spatial frequency of wrapped phase (modulo

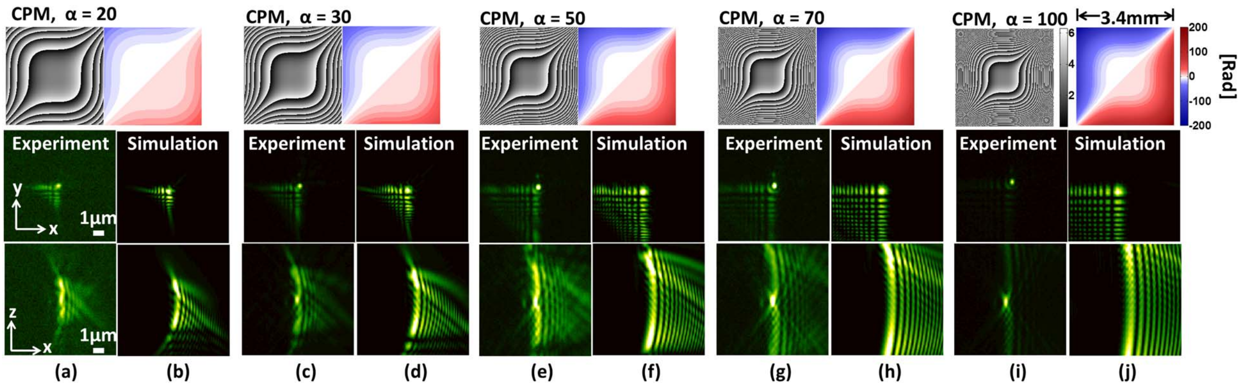

Fig. 4. Effect of reduced SLM modulation depth on the WFE-PSF due to a high density of wrapped phase lines per pixel is demonstrated on experimental CPM WFE-PSFs with varying values of the α design parameter. In the top row, CPM phase masks for different α are shown for each case (wrapped on the left and unwrapped on the right). XY section images and XZ section images are shown, respectively, in the middle and bottom row for different design parameter values: (a,b) $\alpha = 20$; (c,d) $\alpha = 30$; (e,f) $\alpha = 50$; (g,h) $\alpha = 70$; and (i,j) $\alpha = 100$. Lens, 63×, 1.4 NA; wavelength, 515 nm. $\Delta n = 0.05$ between coverslip and mounting medium, point source is located at 25 μm depth below the coverslip. The SLM can implement a limited number of wrapped phases (0–2π), i.e., a limited maximum phase delay, depending on the aperture size, pixel size, and cross-talk effects.

2π) in the computed phase mask approaches the SLM limits, in terms of cross talk and the number of wrapped phase per SLM pixel, the phase modulation of the implemented mask is reduced [32], thereby reducing its diffraction efficiency. Conversely, light that is not diffracted by the SLM is still diffracted by the aperture of the microscope.

A consequence of the SLM response is an intensity distribution in the measured PSF that appears to be unmodulated: for example, as seen in the axial intensity of the XZ view of the CPM-PSF (Fig. 4, bottom row). This intensity distribution is associated with the CCA-PSF. Superposition of simulated CCA and WFE-PSF intensities produces a similar result. At low values of α, the intensity of the CCA-associated intensity is negligible [Fig. 4(a)]; at $\alpha = 70$, this intensity is nearly equal to that of the CPM-PSF intensity [Fig. 4(g)], while at $\alpha > 70$ the intensity is high compared with that of the CPM-PSF pattern, which is low [Fig. 4(i)]. That this effect is due to reduced SLM phase modulation rather than aliasing of phase wrapping oscillations is supported by measured PSFs [Fig. 4(c)] for which the wavefront encoding SLM phase mask exhibits no evidence of aliasing [Fig. 3(a)], yet unmodulated intensity distribution is still observed. The discrepancy between the experimental and simulated PSFs, evident in Fig. 4, grows with an increase in the value of α and the related increase in density of wrapped phase lines per pixel. A similar unmodulated intensity distribution attributed to reduced SLM phase modulation is also observed in experimental GCPM- and SQUBIC-PSFs (Figs. 5 and 6). The unmodulated portion can be avoided by addition of a phase ramp to the mask such that wavefront encoding emission is steered away from the zero-order frequency, however this approach further restricts the phase limitations on wavefront encoding parameters and introduces a signal loss.

C. WFE-PSF Measurements and Simulations

Experimentally measured WFE-PSFs show a 3D spatial intensity distribution that is comparable with the simulated intensity for the CPM, GCPM, and the SQUBIC WFE-PSFs within the design parameter bounds discussed in Section 4.B. Although experimental properties of the WFE-PSFs are not in perfect agreement with those predicted by simulation (Fig. 4–6), they confirm basic properties of the PSF that are consistent with the function of the phase mask design. In the case of CPM for $\alpha = 30$ and SQUBIC phase mask for $A = 50$, quantitative comparison (Table 1) predicts that the level of agreement between experimental and simulated PSFs is similar to that of the conventional CCA PSF. This comparison generally improves when SLM effects on the phase mask implementation are taken into account in simulation. The largest observable differences between measured and simulated PSFs are: (1) the effects of experiment-related noise, due to low fluorescent signal; (2) the influence of an intensity distribution that appears to be unmodulated during wavefront encoding [Figs. 4(c), 4(e), 4(g), and 4(i), as well as Fig. 5]. These results are also observed

Table 1. Comparison of Experimental and Simulated PSFs

Discrepancy Measure	Phase Mask	Exp. PSF vs. Sim. PSFs at depth	Exp. PSF vs. SLM-based Sim. PSFs at depth
I-divergence	CCA	2.55×10^6	NA
	CPM $\alpha = 30$	3.20×10^6	3.16×10^6
	SQUBIC $A = 50$	2.15×10^6	1.65×10^6
	GCPM $\beta = -\alpha = 50$	1.42×10^7	1.53×10^7
Correlation coefficient	CCA	0.6970	NA
	CPM $\alpha = 30$	0.5876	0.7027
	SQUBIC $A = 50$	0.4361	0.4983
	GCPM $\beta = -\alpha = 50$	0.2755	0.2816

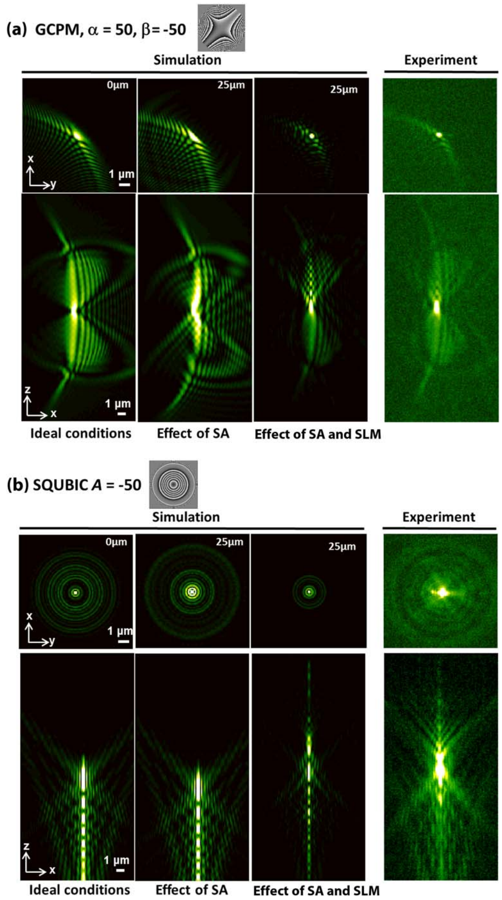

Fig. 5. 3D WFE-PSF intensities (used for quantitative comparison, Table 1) show good agreement between experiment and simulation at 25 μm below the coverslip when the response of the SLM is simulated. Comparison of experiment with simulation of a point source at both 0 μm (ideal conditions) and 25 μm depths below the coverslip highlights the effect of SA on the designed properties of the WFE-PSFs using the (a) GCPM and the (b) SQUBIC phase mask. In each case, the lateral (XY) view (top row) is shown at the best focus axial location, while corresponding axial (XZ) view (bottom row) is shown for $y = 0$. Experimental images are displayed using different intensity scales and are saturated to show low-intensity details of the diffracted signal. Simulated and experimental PSFs are computed and acquired with a 63×, 1.4 NA oil-immersion lens and a 515 nm wavelength.

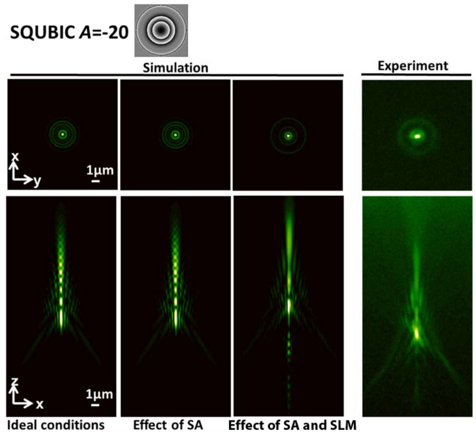

Fig. 6. Effect of change in sign of SA and varying design parameter A in the SQUBIC phase mask design. XY section images (top row) and XZ section images (bottom row) from the center of the SQUBIC-PSFs. A lower A value reduces the number of 0–2π wrapped phase cycles in the SQUBIC phase mask (top row) and decreases the PSF's axial extent compared to the PSFs in Fig. 5(b). PSFs are computed and measured with SA, which is opposite in sign to the aberration in PSFs shown in Fig. 5. This sign change is induced by a change in mounting medium (i.e., by a change in the RI difference), but qualitative agreement, between measured and computed PSFs, remains. Experimental images are displayed using different intensity scales and are saturated to show low-intensity details of the diffracted signal. Lens: 63×. Wavelength: 515 nm.

in comparisons between PSFs computed and measured in a sample with a mounting medium RI greater than the immersion medium RI such that the induced SA is reversed in sign (Fig. 6).

Measures of I-divergence and correlation coefficient are compared for simulated and experimentally measured PSFs of the CCA microscope and WFE-PSFs. Specifically, the experiment is compared with: (1) simulation using the theoretical phase mask, and (2) simulation using an SLM-modified mask (see Section C). Comparison of CCA-PSFs provide reference values that represent a match between observed and predicted data for the case of a model that is known to work well with algorithms developed to produce accurate solutions to the inverse imaging problem. I-divergence and correlation coefficient measures of the CCA-PSFs are in the same order of magnitude as those for CPM and SQUBIC WFE-PSF cases (Table 1). The GCPM I-divergence measure is higher than the other two cases. In the case of CPM for $\alpha = 30$ and SQUBIC for $A = 50$, the I-divergence is reduced, and the correlation coefficient is increased when the experimental PSF is compared with the simulated SLM-modified PSF. In the case of GCPM $\beta = -\alpha = 50$, these measures increase (~8% in I-divergence and ~2% in correlation coefficient).

1. CPM-PSF ($\alpha = 30$)

The CPM-PSF ($\alpha = 30$) curvature along the axial direction and away from the nominal focus, seen in the experimental PSFs (Fig. 4), confirms previously reported simulation results [1,2]. The axial curvature of the CPM-PSF decreases with increasing value of the parameter α, in Eq. (1), as predicted by theory [2]. Simulated CPM-PSFs indicate the expected effect of SA, i.e., intensity asymmetry along Z [Figs. 4(a) and 4(c)], which results due to RI difference, $\Delta n = 0.05$, at the coverslip to mounting medium interface and the location of the point light source at 25 μm depth below the coverslip. The measured CPM-PSFs show comparable effects visible in the XY view (Fig. 4, middle row), in the curvature of the extreme ends of the lateral intensity pattern, and in the XZ view (Fig. 4, bottom row), in the asymmetric axial variation of the lateral intensity pattern. The impact of these SA effects is a reduction in the range of depth-of-field extension.

Experimental results confirm simulations, which indicate that increasing the value of α results in a greater depth of field. Thus, the SLM provides the ability to select the WFE imaging system's depth of field (Fig. 4).

2. GCPM-PSF ($\alpha = 50$, $\beta = -50$)

In contrast, the GCPM-PSF [Fig. 5(a)], with parameters $\alpha = 50$, $\alpha = -\beta$, is intended for COSM of thick samples and is produced by a phase mask design selected to balance sensitivity to misfocus with insensitivity to SA [1]. In fact, the measured GCPM-PSF [Fig. 5(a)], acquired with a point source at the same depth as in the case of the measured CPM-PSF, shows that SA has significantly less of an effect on its shape than on the shape of the CPM or CCA-PSFs. Axial asymmetry of the GCPM-PSF is significantly less pronounced than that of CPM and CCA-PSFs, in both simulation and experiment. The experimental GCPM-PSF [Fig. 5(a)] shows less axial asymmetry than simulation, which may be attributed to its low signal-to-noise ratio. As a result of noise, very low magnitude diffraction effects are not discernible experimentally. However, the scale and spatial variance of the measured diffraction pattern is exactly predicted by simulation. Simulated and experimental GCPM-PSFs exhibit a decreasing axial intensity away from their central peak that characterizes sensitivity to misfocus. This property demonstrates the reduced depth of field of this particular GCPM-PSF, as compared with the CPM-PSF (Fig. 4), making it suitable for COSM.

The parameters of the CPM and GCPM designs are limited by phase stroke before a sampling limitation is reached. The SLM pixel size imposes an upper limit of $\alpha \leq 90$ for the CPM while the limit for the GCPM is upward of $\alpha = -\beta = 150$. For large values of α or β, the maximum phase amplitude of these mask designs exceeds the number of 0–2π wrapped phase cycles that the device can accommodate. For GCPM, the phase stroke of the SLM is not sufficient to implement the GCPM maximum phase amplitude for $\alpha > 150$. For CPM, the phase stroke of the SLM is not large enough to accommodate the CPM maximum phase amplitude for $\alpha > 90$. Note that the SLM phase stroke depends in part on its grid size, and this limitation could be relaxed by introducing magnification in the SLM relay path. However, CPM and GCPM implementation with the SLM is observed to be limited further by high phase wrapping spatial frequency.

3. SQUBIC-PSF ($A = 50$)

The SQUBIC-PSF ($A = 50$) was also proposed to enhance COSM [4,5], but with different properties. Note that this PSF does not extend the depth of field of an imaging system. Its structure is distinguished from CPM and GCPM-PSFs by its lateral rotational symmetry and axial asymmetry. The experimental SQUBIC-PSF [Fig. 5(b)] confirms the lateral confinement of the very brightest part of the simulated SQUBIC-PSF intensity. Also, its asymmetry is consistent with the simulated SQUBIC-PSF. The simulated SQUBIC-PSF has a long axial intensity distribution, punctuated by multiple nulls. The experimental SQUBIC-PSF appears to have at least one minimum between a primary area of brightest intensity and a second area of bright intensity along the axial direction. For $A = 50$ and these simulation parameters, the SQUBIC PSF is almost completely invariant, as judged qualitatively, with the change in SA [Fig. 5(b)].

In the case of SQUBIC-WFE, the range of depth for which the SQUBIC-PSF is invariant can be increased by, respectively, increasing A [5]. This linear scaling factor is limited to $A \leq 88$ by SLM sampling requirement limits rather than phase stroke properties of the SLM. Higher sampling (via increased magnification in the wavefront encoding relay) is required to avoid aliasing of phase wrapping oscillations at the rapidly varying edge of the SQUBIC design [Fig. 5(b)]. PSFs computed and measured indicate that the effect of SA on the SQUBIC ($A = 20$) PSFs is still reduced as compared with CCA in these particular imaging conditions [4,5]. In Fig. 6, simulated and experimental WFE PSFs (SQUBIC $A = 20$) with SA, which is opposite in sign to the aberration experienced by PSFs shown in Fig. 5, are qualitatively in agreement after accounting for the effect of the SLM implementation.

5. CONCLUSION

In this study, we have shown that LC-SLM wavefront encoding phase masks successfully implement a wide range of phase function designs whose potential use in 3D computational optical microscopy is already established via simulation. Interferometry results independently validated the wavefront encoding SLM phase implementation in addition to comparison of measured and numerical WFE-PSFs. These experimentally measured WFE-PSFs confirmed basic properties of the numerical WFE-PSFs, which have been designed for different imaging system properties, specifically EDF and optical sectioning with insensitivity to spherical aberration. Experimental variation of phase mask parameters has verified function-related structure changes in the PSF dictated by these parameters. Thus, GCPM and SQUBIC PSFs, designed to enable depth-invariant optical image acquisition, can be implemented with an SLM and enable nonmechanical switching between EDF and optical sectioning modes of computational microscopy in a single imaging path. PSF design parameters can be tuned and chosen to suit experimental needs.

Practical limitations on switchable phase mask parameters are imposed in part by the SLM format and in part by the angle of light incidence on the SLM in the present configuration. Future implementations may overcome this in part by hardware changes in the SLM relay path or by improved SLM formats, which will allow higher phase modulation efficiency than currently achieved. Incorporation of an empirically determined SLM response in the computation of the PSF model improves the level of quantitative agreement between modeled and experimental WFE-PSFs. Divergence and correlation measures between experimental and simulated WFE-PSFs indicated an improved match between simulation and experiment after accounting for effects of the SLM. Divergence measures between experimental and simulated WFE-PSFs were found to be on the same order of magnitude as those of the experimental and simulated CCA-PSFs for which model-based imaging algorithms are already successful. This suggests a more sophisticated model of the SLM effects on the implemented phase mask may be useful in further improving the match between simulation and SLM-implemented experiments. Yet unknown is whether SLM-modified SQUBIC and GCPM-PSFs fully retain properties, predicted in simulation, that can improve the accuracy of the computational-optical imaging approach to 3D microscopy of objects at depth within thick samples.

Funding. National Science Foundation; Directorate for Biological Sciences (BIO); Division of Biological Infrastructure (DBI) (0844682, 0852847, 1353904).

Acknowledgment. NP acknowledges support through the University of Memphis, Herff College of Engineering graduate fellowship program. AD acknowledges funding from the University of Valencia through the predoctoral fellowship program "Atracció de Talent." The authors thank Dr. A. Linnenberger (Meadowlark Optics, Inc.) for helpful discussions of SLM technology.

REFERENCES

1. S. Yuan and C. Preza, "Point-spread function engineering to reduce the impact of spherical aberration on 3D computational fluorescence microscopy imaging," Opt. Express **19**, 23298–23314 (2011).
2. M. Arnison, C. J. Cogswell, C. J. R. Sheppard, and P. Török, "Wavefront coding fluorescence microscopy using high aperture lenses," in *Optical Imaging and Microscopy: Techniques and Advanced Systems*, P. Török and F.-J. Kao, eds. (Springer, 2003), pp. 143–165.
3. G. Saavedra, I. Escobar, R. Martínez-Cuenca, E. Sánchez-Ortiga, and M. Martnez-Corral, "Reduction of spherical-aberration impact in microscopy by wavefront coding," Opt. Express **17**, 13810–13818 (2009).
4. N. Patwary, A. Doblas, S. V. King, and C. Preza, "Reducing depth induced spherical aberration by wavefront coding in 3D widefield fluorescence microscopy," Proc. SPIE **8949**, 894911 (2014).
5. A. Doblas, S. V. King, N. Patwary, G. Saavedra, M. Martinez-Corral, and C. Preza, "Investigation of the SQUBIC phase mask design for depth-invariant widefield microscopy point-spread function engineering," Proc. SPIE **8949**, 894914 (2014).
6. G. Carles, A. Carnicer, and S. Bosch, "Phase mask selection in wavefront coding systems: A design approach," Opt. Lasers Eng. **48**, 779–785 (2010).
7. W. T. Cathey and E. R. Dowski, "New paradigm for imaging systems," Appl. Opt. **41**, 6080–6092 (2002).
8. S. Quirin, D. S. Peterka, and R. Yuste, "Instantaneous three-dimensional sensing using spatial light modulator illumination with extended depth of field imaging," Opt. Express **21**, 16007–16021 (2013).
9. S. R. P. Pavani and R. Piestun, "Three dimensional tracking of fluorescent microparticles using a photon-limited double helix response system," Opt. Express **16**, 22048–22057 (2008).
10. S. Jia, J. C. Vaughan, and X. Zhuang, "Isotropic three-dimensional super-resolution imaging with a self-bending point spread function," Nat. Photonics **8**, 302–306 (2014).
11. Z. Wang, L. Millet, M. Mir, H. Ding, S. Unarunotai, J. Rogers, M. U. Gillette, and G. Popescu, "Spatial light interference microscopy (SLIM)," Opt. Express **19**, 1016–1026 (2011).
12. S. Bernet, A. Jesacher, S. Fürhapter, C. Maurer, and M. Ritsch-Marte, "Quantitative imaging of complex samples by spiral phase contrast microscopy," Opt. Express **14**, 3792–3805 (2006).
13. M. R. Beversluis, L. Novotny, and S. J. Stranick, "Programmable vector point-spread function engineering," Opt. Express **14**, 2650–2656 (2006).
14. S. Quirin and R. Piestun, "Depth estimation and image recovery using broadband, incoherent illumination with engineered point spread functions," Appl. Opt. **52**, A367–A376 (2013).
15. J. G. McNally, T. Karpova, J. Cooper, and J. A. Conchello, "Three-dimensional imaging by deconvolution microscopy," Methods **19**, 373–385 (1999).
16. X. Xie, Y. Chen, K. Yang, and J. Zhou, "Harnessing the point-spread function for high-resolution far-field optical microscopy," Phys. Rev. Lett. **113**, 263901 (2014).
17. C. Preza and J. A. Conchello, "Depth-variant maximum-likelihood restoration for three-dimensional fluorescence microscopy," J. Opt. Soc. Am. A **21**, 1593–1601 (2004).
18. N. Patwary and C. Preza, "Image restoration for three-dimensional fluorescence microscopy using an orthonormal basis for efficient representation of depth-variant point-spread functions," Biomed. Opt. Express Rev. **6**, 3826–3841 (2015).
19. C. Preza and V. Myneni, "Quantitative depth-variant imaging for fluorescence microscopy using the COSMOS software package," Proc. SPIE **7570**, 757003 (2010).
20. S. V. King, A. Doblas, N. Patwary, G. Saavedra, M. Martinez-Corral, and C. Preza, "Implementation of PSF engineering in high-resolution 3D microscopy imaging with a LCoS (reflective) SLM," Proc. SPIE **8949**, 894913 (2014).
21. I. Escobar, E. Sánchez-Ortiga, G. Saavedra, and M. Martínez-Corral, "New analytical tools for evaluation of spherical aberration in optical microscopy," in *Optical Fluorescence Microscopy* (Springer, 2011), pp. 85–100.
22. E. Dowski and W. Cathey, "Extended depth of field through wave-front coding," Appl. Opt. **34**, 1859–1866 (1995).
23. S. Prasad, T. Torgersen, V. Pauca, R. Plemmons, and J. van der Gracht, "High-resolution imaging using integrated optical systems," Int. J. Imaging Syst. Technol. **14**, 67–74 (2004).
24. D. Engström, M. Persson, and M. Goksör, "Spatial phase calibration used to improve holographic optical trapping," in *Biomedical Optics and 3D Imaging* (2012), paper DSu2C.3.
25. M. Persson, D. Engström, and M. Goksör, "Reducing the effect of pixel crosstalk in phase only spatial light modulators," Opt. Express **20**, 22334 (2012).
26. M. Hossain, S. V. King, and C. Preza, "Enhanced extended depth-of-field microscopy via modeling of SLM effects on the applied phase mask," in *Imaging and Applied Optics, OSA Technical Digest* (2014), paper IW4C.4.
27. B. E. A. Saleh and M. C. Teich, *Fundamentals of Photonics* (Wiley, 1991).
28. S. F. Gibson and F. Lanni, "Experimental test of an analytical model of aberration in an oil-immersion objective lens used in three-dimensional light microscopy," J. Opt. Soc. Am. A **9**, 54–66 (1992).
29. C. Preza, "Computational Optical Sectioning Microscopy Open Source (COSMOS) Software package," Computational Imaging Research Laboratory (CIRL), 2014, http://cirl.memphis.edu/cosmos.php.
30. I. Csiszár, "Why least squares and maximum entropy? An axiomatic approach to inference for linear inverse problems," Ann. Statist. **19**, 2032–2066 (1991).
31. J. Stockley and S. Serati, "Cascaded one-dimensional liquid crystal OPAs for 2-D beam steering," Proc. IEEE **4**, 1817–1822 (2003).
32. S. T. Wu and D. K. Yang, *Fundamentals of Liquid Crystal Devices* (Wiley, 2006).